Transport Effects on Capacitance-Frequency Analysis for Defect Characterization in Organic Photovoltaic Devices

Liang Xu, Jian Wang, and Julia W. P. Hsu

Phys. Rev. Applied **6**, 064020 — Published 28 December 2016

DOI: 10.1103/PhysRevApplied.6.064020

Transport Effects on Capacitance-Frequency Analysis for Defect Characterization in Organic Photovoltaic Devices

Liang Xu, Jian Wang, and Julia W. P. Hsu*

Department of Materials Science and Engineering, The University of Texas at Dallas, 800 W. Campbell Rd., Richardson, TX, 75080, USA

Corresponding Author

* E-mail: jwhsu@utdallas.edu

ABSTRACT: Using capacitance−frequency (C-f) analysis to characterize density-of-states (DOS) distribution of defects has been well established for inorganic thin film photovoltaic devices. While C-f analysis has also been applied to bulk-heterojunction (BHJ) organic photovoltaic (OPV) devices, we show that the low carrier mobility in the BHJ material can severely alter the C-f behaviors and lead to misinterpretations. Due to the complicated nature of disorders in organic materials, artifacts from an erroneous C-f analysis are difficult to identify. Here we compare drift-diffusion simulations with experiments to reveal situations when the validity of C-f analysis for defect characterization breaks down. When a flat-band region is present in the low-mobility active layer, the capacitive response cannot follow the electrical modulation and behaves as if the active layer is a dielectric at frequencies higher than the characteristic frequency determined by carrier mobility and thickness. The transition produces a fictitious shallow defect when defect analysis is applied. Even in fully depleted devices, the defect distributions derived from C-f analysis can appear at spuriously deeper energies if the mobility is too low. Through simulations, we determine the ranges of mobility and thickness for which the C-f analysis can effectively yield credible defect DOS information. Insight from this study also shed light on transport limitation when using capacitance spectroscopy for defect characterization in general.

1. INTRODUCTION

Defect states are well-known to plague organic photovoltaic devices (OPVs) by increasing charge recombination, deteriorating charge transport, and increasing exciton annihilation [1-4]. Accurate defect state characterization is thus critical in OPV research. Several techniques, such as capacitance-frequency (C-f) analysis [5], deep-level transient spectroscopy [6], thermally stimulated current [7], and current density-voltage (J-V) modeling [8] have been used to identify defect distribution in OPVs. It is well known that the presence of defects modifies the frequency-dependent capacitance behavior [9-11]. The C-f analysis was first applied to investigate the defect state energy and distribution in inorganic thin film photovoltaic devices by Walter et al. [12] and Hegedus et al [13], and recently adapted to characterize defect states in OPVs[5,14-19] and perovskite photovoltaic devices [20,21]. Another approach is to perform capacitance-voltage (C-V) measurements under a few frequencies [11,22]. but this method can only roughly estimates the total defect state density, not defect energetics obtained in C-f analysis.

In order for C-f analysis to probe the capture/emission process of defect states with characteristic frequencies corresponding to their energy positions within the band-gap, the capacitive response of the mobile carriers must be frequency independent over the entire measurement frequency range (typically 0.1 Hz – 1 MHz). Generally, this assumption is valid for inorganic materials, which usually have the mobility higher than 1 $cm^2V^{-1}s^{-1}$ [23,24]. However, for the bulk-heterojunction (BHJ) type OPVs where charge transport heavily relies on hopping processes, their effective charge mobility is usually lower by orders of magnitude (10^{-3} – 10^{-7} $cm^2V^{-1}s^{-1}$), especially at low temperatures [25-27]. Under such circumstances, conducting carriers become unresponsive at high

frequencies, and the frequency dependence of capacitance is severely altered. As a result, artifacts can arise from applying the same defect reconstruction from C-f data as in inorganic studies without careful examination. Moreover, due to the complicated nature of disorders in organic materials [28], spurious results due to transport are hard to be distinguished from real defects, and thus misinterpreted. In the literature, several studies have not considered the effect of low mobility in BHJ OPVs with published results susceptible to transport related artifacts [14-19]. To the best of our knowledge, no research on the effect of limited charge transport on defect characterization using C-f analysis has been done.

In this study, we elucidate the transport effect on C-f analysis by performing experimental studies of OPVs with varying thickness and mobility and comparing the results with drift-diffusion simulations. An inevitable transition from depletion capacitance to geometric capacitance is demonstrated in devices with a flat-band region, which correspondingly introduces a fictitious shallow level into the derived defect density of states (DOS). Even in fully depleted devices, the low mobility leads to more reduction of capacitive response from real defects at higher frequencies, therefore, a shift of the defect distribution to spuriously deeper energies which do not accurately reflect the real defect position. Finally, we establish a zone of confidence in terms of mobility and thickness ranges where accurate defect characterization by C-f analysis can be achieved. Insight from this study also sheds light on the effect of transport on performing capacitance based defect characterization on devices and materials in general beyond OPVs, especially at low temperatures.

2. BACKGROUND

Using C-f analysis to determine the defect state DOS distribution in photovoltaics was initially established by Walter et al. [12] and Hegedus et al. [13]. This method consists of calculating the derivative of the junction capacitance with respect to the angular frequency of the ac modulation, which is corrected by a factor accounting the band bending and the drop of the modulation signal over the space charge region of the junction. Figure 1 (a) demonstrates the band diagram of a fully depleted semiconductor, simulating the active layer of a BHJ OPV device in the dark at equilibrium (zero voltage bias). A band bending develops across the active layer as the Fermi level (E_f) of the electrodes aligns with the E_f of the semiconductor. In this study, we consider hole traps with peak energy at E_0 between the mid-gap and valence band edge (E_v, or highest occupied molecular orbital (HOMO) in organic semiconductors), since OPVs are typically p-type doped [7,29-31]. The occupation of such a defect level at a given spatial position is determined by its energy with respect to the local E_f as shown in Figure 1(a), with M denoting the position where E_0 equals E_f. Due to the presence of the band bending, all the states spatially to the right of M (above E_f) are occupied by holes (filled hole traps, indicated by the solid line), while all the states to the left of M (below E_f) are not occupied by holes (empty hole traps, indicated by the dashed line). In the capacitance measurement, a small perturbation of the ac voltage effectively modulates the occupation of the defect states at M, i.e., capture and emission of holes from these states, which in turn contributes to the junction capacitance.

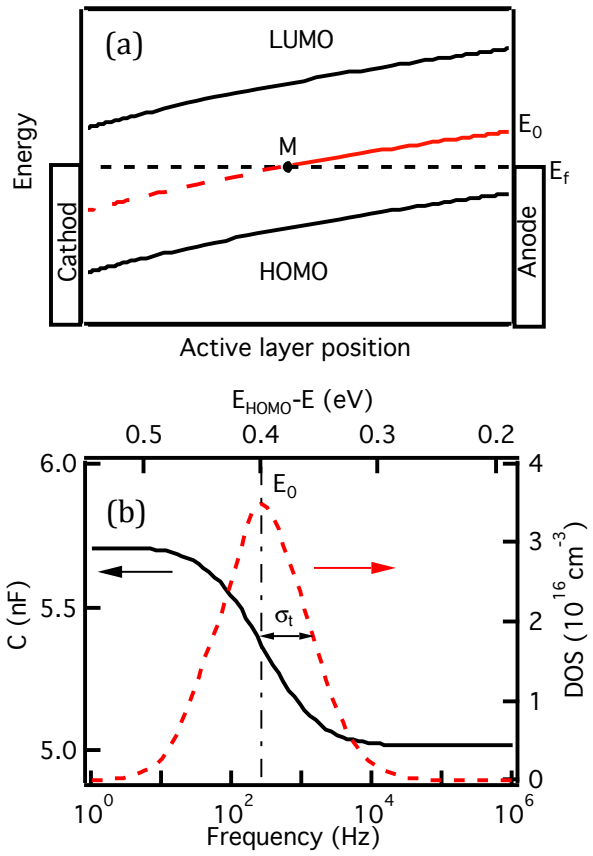

FIG. 1. (a) Schematic band diagram of a *p*-doped device in dark at zero bias voltage. The crossing point between the Fermi level E_f and the defect energy E_0, M, within the depletion zone marks the position of the occupancy change. (b) C vs. f in the dark at zero bias (black solid line) of the device shown in (a) and the corresponding defect DOS distribution (red dashed line) derived from C-f spectrum using Equation 3, which has a Gaussian distribution with a peak energy at E_0 and a disorder width σ_t.

For the defects acting as hole traps, the characteristic time τ of thermal emission from a defect state residing within band-gap to the valence band is given by [13]

$$\tau = \gamma^{-1} \exp(\frac{\Delta E}{k_B T}) \quad (1)$$

where $k_B T$ is the thermal energy, γ is the attempt-to-escape frequency ($\gamma = \upsilon_{th} \sigma_p N_v$,

where υ_{th} is the thermal velocity, σ_p is the hole capture cross section, and N_v is the valence band effective density of states), and ΔE is the difference between the defect energy level and the valence band edge ($\Delta E = E_v - E_0 > 0$). $1/\tau$ sets the maximal frequency at which the defect states are still able to respond to the ac modulation and contribute to the junction capacitance. The condition $\omega\tau = 1$ ($\omega = 2\pi f$ is the angular frequency of the ac modulation while f is the measurement frequency) occurs at ω_E, which corresponds to a demarcation energy E_ω:

$$E_\omega = \Delta E = k_B T \ln(\frac{\gamma}{\omega_E}), \quad (2)$$

E_ω defines the energy level (relative to E_v) of defect states that can respond when subjected to ac modulation with angular frequencies lower than ω_E. Thus, each capacitance transition corresponds to a distinct defect state with demarcation energy corresponding to the transition frequency according to Equation 2.

To probe the entire defect spectrum, the frequency of the ac modulation is varied from 1 to 10^6 Hz and Equation 2 is applied to obtain all demarcation energies associated with different defect states. In this approach, it is assumed that the frequency dependence of the junction capacitance is only determined by the defect emission rate, so the capacitance spectrum reflects the defect energy landscape, with high frequencies corresponding to energy levels near the valence band and sweeping towards mid-gap as the frequency decreases. The defect DOS distribution is further taken to be proportional to the derivative of the capacitance with respect to the frequency as [12]:

$$DOS(E_\omega) = -\frac{V_{fb}\omega}{qdk_BT}\frac{dC(\omega)}{d\omega}, \quad (3)$$

where q is the magnitude of elementary charge, d the depletion region width, and V_{fb} the flat-band potential. For a defect with a peak DOS at E_0, Figure 1(b) shows its C-f behavior (black solid line) and corresponding defect DOS distribution derived from the C-f specrum (red dashed line), which is typically analyzed by a Gaussian function:

$$DOS(E) = \frac{N_t}{\sqrt{2\pi\sigma_t^2}}\exp[-\frac{(E_0 - E)^2}{2\sigma_t^2}], \quad (4)$$

where σ_t is the disorder width and N_t is the total defect density.

3. EXPERIMENTAL DETAILS

3.1. Device Fabrication

All chemicals were purchased from Fisher Scientific and used as received, and all processing was performed in a N_2 glove box (Innovative Technology) unless otherwise noted.

Inverted BHJ devices were fabricated on patterned indium tin oxide (ITO; Xinyan, 15 Ω/square). A ZnO electron transport layer (ETL, ~30 nm) was spin- coated at 2000 rpm in air using a solution having 0.5 M of zinc acetate dihydrate and 0.5 M of monoethanolamine dissolved in a 2-methoxyethanol, and then was pyrolyzed at 300°C for 10 min in air. For the BHJ active layer, poly (3-hexylthiophene) (P3HT, RMI-001E, Rieke Metals, Inc.) and [6,6]-phenyl C61-butyric acid methyl ester ($PC_{61}BM$, Solenne BV) were dissolved in anhydrous chlorobenzene (CB, Sigma-Aldrich) at varying concentrations from 8 to 32 mg/mL and spin-coated at varying spin speed between 700

and 1500 rpm to obtain different thicknesses. All films were annealed at 170°C for 10 min in N_2 after deposition, and a 7 nm MoO_3 hole transport layer (HTL) and a 100 nm Ag electrode were thermally evaporated (Angstrom Engineering) to complete the devices, with a junction area of 0.11 cm^2 each.

For the conventional fullerene-based devices, 30 nm of poly(3,4-ethylenedioxythiophene):poly(styrenesulfonate) (PEDOT:PSS) (Heraeus Clevios AI 4083) was spin coated onto pre-cleaned ITO substrates followed by 140 °C annealing in N_2 for 10 min to form the HTL. P3HT and [6,6]-phenyl C71-butyric acid methyl ester ($PC_{71}BM$, Solenne BV) with a total concentration of 25 mg/mL were dissolved overnight in CB solution with varying P3HT concentrations between 1 and 20 wt.%. Active layer thicknesses between 60 - 70 nm were spin-cast at 1500-4000 rpm (to keep film thickness constant for all P3HT concentrations) for 60s. All active layers were annealed at 70 °C in N_2 for 10 min after deposition. Finally, Ca (7 nm) and Al (100 nm) were thermally evaporated to complete the devices. For the hole-only devices MoO_3 (7 nm) and Ag (100 nm) were thermally evaporated following the active layer.

3.2. Device characterization

The *J-V* measurements were performed in a N_2 filled glovebox under AM1.5G 100 mW/cm^2 illumination from a class AAA solar simulator (Abet Technologies) using a low-noise sourcemeter (2635A, Keithley) controlled by a LabView program. The solar simulator intensity was set using a NIST-traceable calibrated photodiode (Abet RR_227KG5). A 2.5 mm diameter aperture was placed in front of each device to rigorously define the illumination area of 0.049 cm^2.

Impedance spectroscopy (IS) measurements used for extracting capacitance value

were carried out in an O-ring sealed sample holder containing N_2 at room temperature using a Zahner IM6 electrochemical workstation. They were performed in dark with an ac bias (20 mV) modulating between 1 Hz and 1 MHz.

4. EXPERIMENTAL RESULTS AND DISCUSSIONS

4.1. Effect of flat-band region on defect characterization

It has been well documented that the active layer of OPVs is typically a moderately p-doped material with a background carrier density from 5×10^{15} to 7×10^{16} cm^{-3} [7,29-31]. The p-type doping is typically unintentional and caused by oxygen, moisture and/or impurities acting as p-type dopants [7,31,32]. Meanwhile, 200 – 300 nm has been established as the optimal active layer thickness in several BHJ systems.[33-37] However, due to partial screening of the built-in electrical field by background carriers, the depletion region of active layer is usually limited to < 150 nm, leaving a non-negligible flat-band (field free) region [30,31,35,38].

P3HT, the most well-studied polymer in OPVs, is known to be p-type doped with a background carrier density of 5×10^{15} to 5×10^{16} cm^{-3} [5,7,39]. While the optimal thickness for P3HT:PC_{61}BM OPVs is ~ 200 nm [33], devices with thickness varying between 100 [38] and 800 nm [40] have been studied. To understand how the flat-band region impacts defect characterization, we investigate the C-f behavior (at dark and zero bias) in inverted ITO/ZnO/P3HT:PC_{61}BM/MoO_3/Ag devices with active layer thickness varying between 55 and 500 nm (Figure 2(a), see Figure S1 and Table S1 for J-V characteristics).[41] The capacitance value is extracted from the IS measurements [42]:

$$C = -\frac{1}{\omega}\left[\frac{Z'' - \omega L}{(Z' - R_s)^2 + (Z'' - \omega L)^2}\right], \quad (5)$$

where Z' and Z'' are the real (in phase) and imaginary (out of phase) components of the measured impedance, respectively, R_s is the series resistance, and L is the parasitic inductance. Notice that within the common frequency range of IS measurement (10^{-1} - 10^6 Hz), while L can usually be ignored, R_s should always be measured (the value of Z' at 1 MHz is used for R_s in our study as shown in Table S1) and included in Equation 5 to obtain an accurate capacitance value [42,43]. Capacitance at high frequency decreases severely without the R_s correction, deviating from its real value (Figure S2).

All devices with varying thickness show continuous decrease in capacitance with increasing frequency below 100 Hz (red dashed ellipse in Figure 2(a)), indicating the existence of deep defect states. In the frequency range between 100 Hz and 1 kHz, all C-f curves exhibit a plateau, which decreases monotonically with increasing active layer thickness and saturates for thicknesses greater than 225 nm. The saturated capacitance plateau value reflects the maximum depletion region width, which is approximately 130 nm with C = 2.7 nF at 1 kHz and z = $3.6\varepsilon_0$ (Table S1) for these devices. Hence, while the two thinnest devices are completely depleted, there must exist a flat-band region in the active layer for the three thicker devices. In these devices, there is an additional step decrease of capacitance (black dashed ellipse in Figure 2(a)) at higher frequencies (> 10 kHz), which is associated with the transition from junction capacitance (C_d) to geometric capacitance (C_g) with a characteristic frequency ω_t. C_d originates from the charges accumulated at the two boundaries of depletion region, which have to transport throughout the quasi-neutral flat-band region to contribute to the capacitance signal,

while C_g stems from the dielectric response of the material, i.e. local movement of charges with net charges at the two electrodes. Such capacitance transition is due to carrier freeze-out in the quasi-neutral flat-band region with poor conductivity, and details can be found in Supplemental Material (Figure S3) as well as previous publications [24,44].

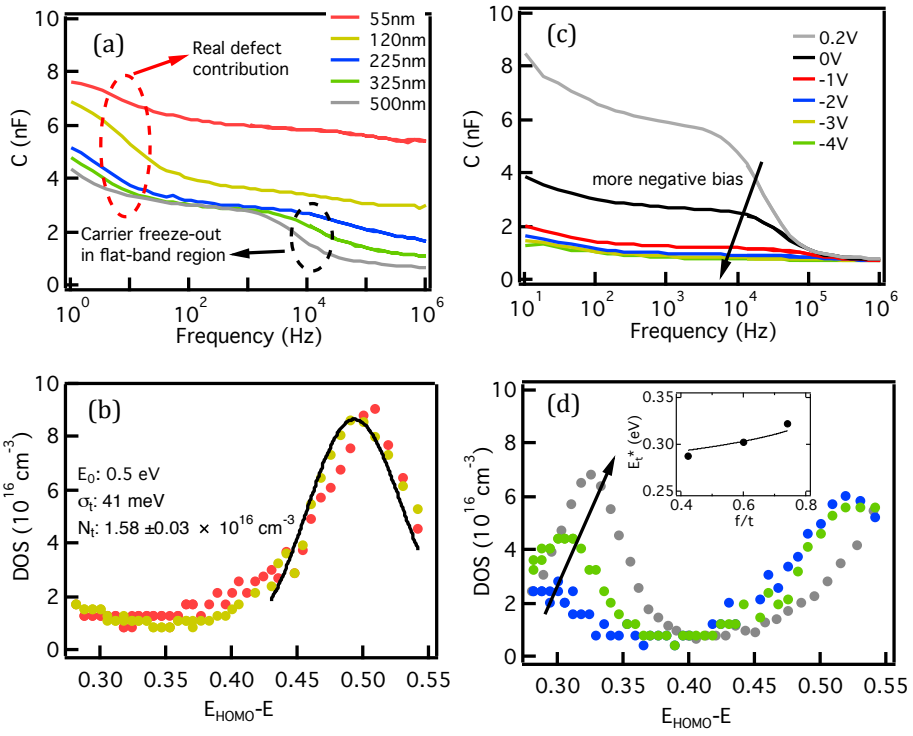

FIG 2. (a) C vs. f in the dark at zero bias for inverted P3HT:PC_{61}BM devices with different active layer thicknesses: 55 nm (red), 120 nm (dark yellow), 225 nm (blue), 325 nm (green), and 500 nm (grey). DOS of defect states derived from C-f analysis for 55 nm and 120 nm devices The solid line in (b) shows the Gaussian fit of the defect DOS according to Equation 4; the corresponding fitting parameters are shown as the inset. (c) C vs. f for a 500 nm thick P3HT:PC_{61}BM device under different biases: 0.2 V (gray), 0 V (black), -1V (red), -2 V(blue), -3 V (dark yellow), and -4 V (green). (d) DOS of defect states derived from C-f analysis for 225 nm, 325 nm, and 500 nm devices. All color schemes used in (b) and (d) are the same as in (a). The inset of (d) depicts the spurious shallow defect peak position E_t* vs. f/t for the three thicker devices with a fit according to Equation 9.

Figure 2(b) demonstrates the defect DOS distributions of the fully depleted 55nm and 120 nm devices derived from the C-f analysis using Equation 3. Very similar DOS distributions located at ~ 0.5 eV are observed in these two devices. When fitted with Equation 4, E_0 = 0.5 eV, a σ_t = 41 meV, and a N_t = 1.58 ± 0.03 ×10^{16} cm^{-3} are obtained (black line in Figure 2(b)), which are in good agreement with previous published results [5].

To further verify that the step decrease of capacitances at higher frequencies (> 10 kHz) in the 225 – 500 nm devices is due to the existence of a flat-band region in the active layer, we perform the C-f measurement under different dc voltage biases. Figure 2(c) illustrates the C-f behavior of a 500-nm P3HT:$PC_{61}BM$ device under bias from 0.2 V to -4 V. With increasing negative bias, the depletion width approaches the entire active layer thickness. As a result, C_d becomes closer to C_g, and thus the capacitance transition gradually disappears. Figure 2(c) unambiguously shows that the capacitance value above 10^5 Hz for all biases is C_g, while C_d can only be measured below 10^4 Hz (also see Figure S4); correspondingly, the transition between 10^4 and 10^5 Hz is not due to defects. However, if one were to apply Equation 4 to the entire C-f spectra, a fictitious defect corresponding to the C_d-to-C_g transition at high frequency (black dashed ellipse in Figure 2(a)) appears at ~ 0.3 eV in the 225 – 500 nm devices (Figure 2(d)). Additionally, the peak energy of the fictitious defect distribution (E_t*) shifts to higher energy, corresponding to lower characteristic frequency, with increasing active layer thickness. The dependence of E_t* on the fraction of flat-band region in the active layer is further examined:

$$E_t^* = k_B T \ln\left(\frac{\gamma\varepsilon}{qp\mu_h\left(1-\frac{f}{t}\right)}\right). \quad (6)$$

where ε is the dielectric constant of the active layer, p is the hole carrier concentration, μ_h is the hole mobility, , f is the width of flat-band region, t is the total thickness of the active layer ($t = d + f$). See Supplemental Material (Equation S3 and related discussion) for detailed derivation. As shown in the inset of Figure 2(d), fitting E_t* for devices with different *f/t* yields a reasonable μ_h = 7 $\times 10^{-5}$ $cm^2 V^{-1}s^{-1}$ [45], given that p is determined to be 5.8 $\times$ 10^{15} cm^{-3} (Figure S4), ε is set to be 3.6ε_0 (Table S1), and a γ of 10^{10} s^{-1} is adopted. While an accurate measurement of γ is difficult in BHJ OPVs (We will discuss more in detail later in this paper), values ranging from 10^7 to 10^{10} s^{-1} are generally used/reported in literatures [16,18,46]. Such a variation of γ only results in an untertainty of ±90 meV in the *absolute* energy position of the defects according to Equation 2, without affecting the DOS distribution. Since we are not studying accurate determination of defect energy positions in this paper but to elucidate the effect of poor transport, a physically reasonable γ value of 10^{10} s^{-1} is adequate for the purpose.

Next, we use the SCAPS 1D drift-diffusion simulator developed by the group of Prof. Burgelman at the University of Gent [47-49] to simulate the μ_h effect on C_d to C_g transition and corresponding artifact in defect characterization by C-f analysis. No actual defect is assumed in the simulations. Based on a 225 nm device with a flat-band region ~ 90 nm (Figure S5(a)) and varying μ_h from 10^{-3} to 10^{-6} $cm^2V^{-1}s^{-1}$, a range typically found in BHJ materials [25], the simulations all show a capacitance transition (Figure 3(a)), which translates to a fictitious shallow defect state (Figure S5(b)). The peak energy of

these fictitious defects (E_t*) is plotted as a function of μ_h (Figure 3(b)), from which a logarithmic decrease of E_t* with increasing μ_h is observed. These results indicate that applying defect characterization using C-f analysis to OPV system with a flat-band region, the capacitance transition from C_d to C_g and hence fictitious shallow defect states would be unavoidable.

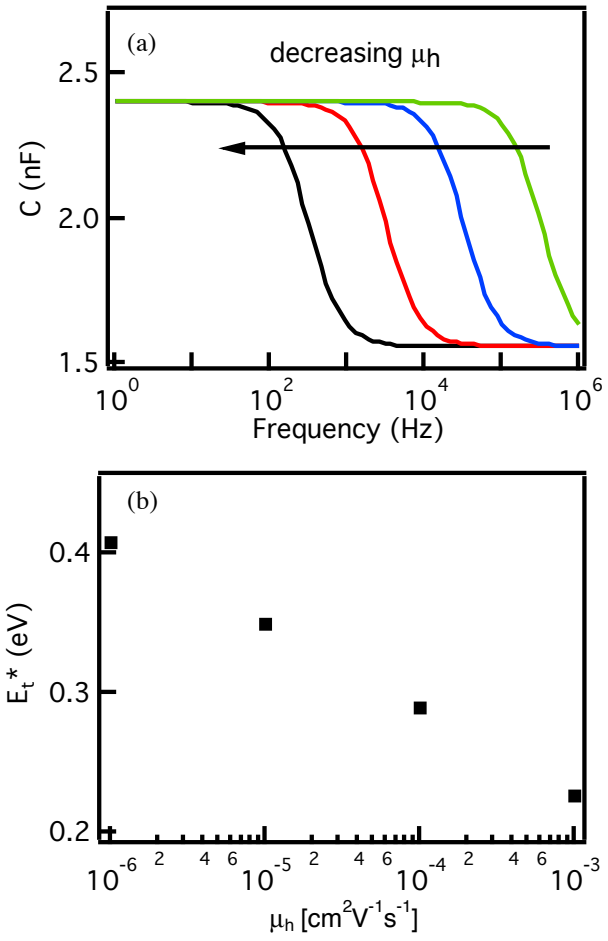

FIG. 3 The simulated fictitious shallow defect position E_t* for a 225 nm device with p = 5.8 × 10^{15} cm^{-3} and hole mobility varying from 10^{-6} $cm^2V^{-1}s^{-1}$ to10^{-3} $cm^2V^{-1}s^{-1}$. Inset: C vs. f for different mobilities: black (10^{-6} $cm^2V^{-1}s^{-1}$), red (10^{-5} $cm^2V^{-1}s^{-1}$), blue (10^{-4} $cm^2V^{-1}s^{-1}$), and green (10^{-3} $cm^2V^{-1}s^{-1}$).

While the existence of shallow defects as band-tail states are well known in OPVs [50,51], based on this study, we caution that misinterpretations might be present in

published literatures and emphasize that care should always be taken when interpreting high frequency capacitance decrease in the C-f analysis of OPV devices [14-19]. Performing C-f measurements under varying biases, as shown in Figure 2(c), provides an effective approach to probe the existence of flat-band region, and therefore is recommended to ensure C_d is correctly measured before extracting defect DOS.

4.2. Effect of low hole mobility in fully depleted devices

Recent high performance OPVs mostly use relatively thin (~100 nm), and therefore fully depleted, active layers to ensure good charge collections [52,53]. To further assess the effect of hole mobility in fully depleted devices, which doesn't manifest the fictitious shallow defect due to the C_d-to-C_g transition (Figure 2), we investigate the $PC_{71}BM$-based OPVs with small amounts of P3HT (see Figure S6 and Table S2 for J-V characteristics) [54]. As shown in Figure 4(a), in all P3HT concentrations, capacitance decreases as frequency increases; additionally, with decreasing P3HT concentration, the capacitance decrease shifts to lower frequency. The capacitance values shown are normalized to the value at 1 MHz, i.e., the C_g, to remove the contribution from thickness variation (see Figure S7(a) for the non-normalized capacitance data). As a result, the corresponding defect state distributions derived from the C-f data (normalized to peak value for clear comparison) show a large variation in energy: with decreasing P3HT concentration, the defect DOS distribution shifts towards mid-gap (Figure 4(b), see Figure S7(b) for DOS before normalization). To understand this phenomenon, we first measure the hole mobility (Figure S8) on hole-only devices (ITO/ PEDOT:PSS/active layer/MoO_3/Ag) following the space-charge limited current (SCLC) modeling [55]. We

find that the hole mobility is strongly dependent on the donor concentration in the fullerene-based devices (Table S3), consistent with published literatures.[56-58] While the μ_h of the 1 wt.% P3HT device (7.0×10^{-7} $cm^2V^{-1}s^{-1}$) is close to the value of pristine $PC_{71}BM$,[56] it is two orders of magnitudes higher in the 20 wt.% P3HT device (3.0×10^{-5} $cm^2V^{-1}s^{-1}$).

While the capacitance of a dielectric is due to its polarization by the applied field, the defect-induced capacitance involves charge transport. In response to the electrical modulation, displacement current is generated from charges emitted from defects and results in an effect on junction capacitance. Therfore, an effective C-f defect characterization is realized only when the average charge transit time in the device τ_d is much shorter than 1/ ω ($\tau_d << 1/\omega$). However, given a μ_h of the order of 10^{-6} $cm^2V^{-1}s^{-1}$, τ_d is of the order 10^{-5} s in a ~100 nm thick device, and thus $\tau_d << 1/\omega$ is no longer satisfied at frequencies higher than 10 kHz. Consequently, contribution to junction capacitance from charges emitted from defect states is reduced in the way that the capacitance decreases more at higher frequency.

To quantify this observation, we simulate the mobility effect on the defect characterization in devices with varying μ_h ($7.0 \times 10^{-7} - 3.0 \times 10^{-5}$ $cm^2V^{-1}s^{-1}$). We introduce a defect DOS with a constant Gaussian distribution into the simulation at $E_{t,0}$ = 0.26 eV (see Figure S9 for details). With the same input defect DOS, the simulations reproduce the trend in C-f behavior with capacitance decrease shifting to lower frequency (Figure 4(c)), and the corresponding defect energy shifting towards deeper energy with decreasing μ_h (Figure 4(d)). Therefore, the shifts of the extracted defect distributions in Fig. 4(b) are artifacts from the C-f analysis arising from the limited transport of holes.

Given that all devices have the same materials, P3HT and $PC_{71}BM$, the defect is expected to have the same energy level in all devices. Indeed, our previous work shows that the energetics measured from the low energy quantum efficiency spectroscopy is the same in all devices with varying P3HT concentration [54]. The experimental studies together with the simulation results indicate that, even in fully depleted thin devices, the low mobility can introduce artifacts and spurious measurements of defect energy position. Note that, for the thicker devices shown in Figure 3, the real defect position has shifted to > 0.5 eV (Figure 2 (d)), a consequence of the same limited charge transport effect discussed here.

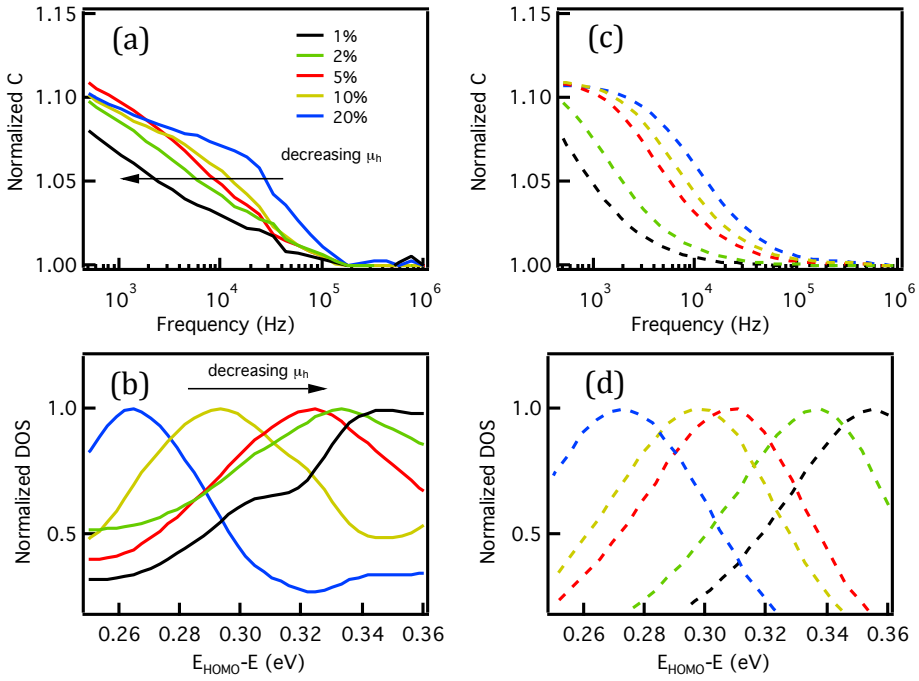

FIG. 4 (a) C vs. f of the fullerene-based OPVs with different P3HT concentration: 1 wt.% (black), 2 wt.% (green), 5 wt.% (red), 10 wt.% (dark yellow), and 20 wt.% (blue). All results are normalized to the value at 1 MHz. The arrow indicates the shift of C-f with decreasing μ_h (P3HT concentration). (b) Defect DOS distributions extracted from (a). All results are normalized to their peak value to emphasize the energy position change. The arrow indicates the shift to deeper position in device with decreasing μ_h (P3HT concentration). (c) Normalized C-f simulated for the fullerene-based OPVs with different μ_h values that

correspond to P3HT concentrations. (d) Corresponding simulated defect DOS distributions (normalized). All color schemes used in (b), (c), and (d) are the same as in (a).

Table 1 Material parameters used for drift-diffusion simulation

Parameters	Symbol [Unit]	BHJ device	Fullerene-Based device
Electron affinity	E_A [eV]	3.7 [59]	
CB & VB effective density of states	$N_{n,p}$ [cm^{-3}]	1×10^{20} 1[29]	
Anode work function	$E_{WF,A}$ [eV]	Aligned with active layer Fermi level	
Cathode work function	$E_{WF,C}$ [eV]	4.0 [59]	
Bimolecular recombination coefficient	k [cm^3s^{-1}]	2×10^{-12} [39]	
Electron mobility	μ e [$cm^2V^{-1}s^{-1}$]	2×10^{-3} [39]	
Background hole concentration	p [cm^{-3}]	5.8×10^{15}	
Relative permittivity ε	ε	3.6	4.5 [54]
Effective bandgap	E_g [eV]	1.1[29]	1.45 [39]
Electron & hole capture cross section	$\sigma_{n,p}$ [cm^2]		1×10^{-17} [a]
Maximum of the defect distribution	$E_{t,0}$ [eV]		0.26[b]
Disorder of the defect distribution	σ_t [meV]		22[b]
Total defect density	N_t [cm^{-3}]		6.02×10^{15} [b]

[a] The hole & electron capture cross section was reported to be within in the range of 1×10^{-18} -1×10^{-16} cm^{-2} [18,60]
[b] Use the adjusted experimental value of 20% P3HT device. See Figure S9 for details.

Figure 5 depicts simulation results that show the combined effects of hole mobility and active layer thickness on the validity of defect characterization using the C-f method. The μ_h value (y axis) is varied within the range (1×10^{-7} - 1×10^{-3} cm^2 V^{-1} s^{-1}) [25], while the thickness t (x axis, 50 – 130 nm) is set within the range of a fully depleted active layer (based on the result of different thickness devices in Figure 2(a)), which also covers the range most relevant to high performance OPVs [52,53]. The color indicates the energy position shift, $\Delta E_t = E_{t,s} - E_{t,0}$, where $E_{t,s}$ is simulation output of the energy peak position of the defect DOS distribution. The white line demonstrates a boundary below which there is no artifact, i.e., the C-f analysis can be applied to characterize defect distributions with accuracy (the green area). With decreasing μ_h (moving upwards) and increasing t (moving rightwards), a larger ΔE_t, i.e., a more severe artifact, is observed. The failure of the C-f analysis in this region is due to the long charge transit time set by

the combination of charge mobility and device thickness. While a μ_h in the order of 10^{-5} $cm^2V^{-1}s^{-1}$ still ensures accurate defect characterizations by C-f analysis in devices with active layer thinner than 60 nm, generally $\mu_h \sim 10^{-4}$ $cm^2V^{-1}s^{-1}$ is the threshold for using C-f analysis in practical devices with reasonably good performance (~100 nm).

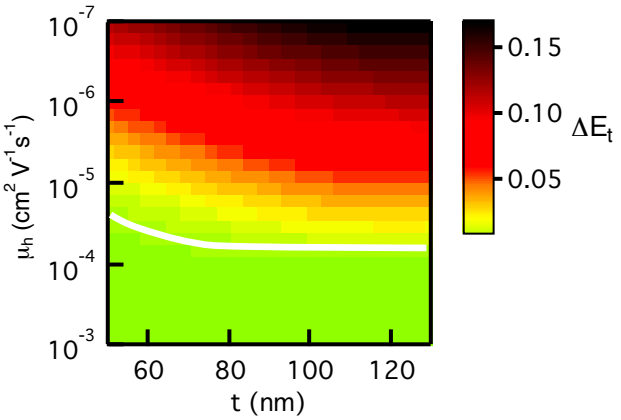

FIG. 5 Simulation results of devices with varying hole mobility (*y* axis) in logarithmic scale and active layer thickness (*x* axis). The color indicates the energy position shift of the defect DOS distributions between the output and input of the simulations. The white line demonstrates a boundary below which there is no artifact.

The transport-limited C-f behavior, as addressed above, further sheds light on the application of other capacitance based techniques for defect characterization. DLTS is commonly used to study defects in semiconductors by measuring a capacitance transient associated with the defect thermal emission [46,61,62]. In the case of low-mobility materials and devices, the frequency used for measuring capacitance should always be carefully evaluated to ensure that the defect contribution is accurately captured by the capacitance measured. More importantly, low temperature measurements are often used in capacitance based defect characterization (including both C-f analysis and DLTS) for obtaining defect activation energy and the attempt-to-escape frequency [18,61-63]. However, in the BHJ OPVs, mobility is reported to decrease by orders of magnitude at

low temperatures [26,27]. Even for the optimized P3HT:PCBM BHJ OPV, which is among the highest mobility OPVs, the mobility drops to 10^{-6} - 10^{-7} cm^2 V^{-1} s^{-1} below 100 K [26]. With such low mobility, the capacitance behavior would be severely altered (Figure 5). As a result, defect activation energy and/or attempt-to-escape frequency obtained from Arrhenius plot can be erroneous. Therefore, to accurately extract these quantities in BHJ OPVs, a better modeling, which takes the temperature dependence of mobility into account, is desired.

5. CONCLUSION

In summary, we have examined the accuracy of defect characterization by C-f analysis in OPVs by comparing experimental data with drift-diffusion simulations. Since the C-f analysis probes the capacitance contribution from the charges emitted from defect states, the C-f analysis is only accurate when all the emitted charges can efficiently respond to the electrical modulation at the measurement frequency (0.1 Hz – 1 MHz). The low mobility in organic materials raises concerns in applying the C-f technique for defect characterization. In an OPV device having a flat-band region in the active layer, a fictitious shallow defect state is found to be inevitable, due to the limited charge transport in the flat-band region that results in the capacitance transition from the depletion to the geometric capacitance within the measurement frequency range. Even in devices with a fully depleted active layer, low mobilities lead to an apparent shift in the derived defect energy position, because the capacitance contribution from defects is more reduced at higher frequencies. Simulations indicate that for a ~100 nm device, using the C-f analysis

to extract defect DOS distributions produce true defect distribution when the hole mobility exceeds 10^{-4} $cm^2V^{-1}s^{-1}$. Thus, special caution should be taken when using C-f analysis for defect characterization in OPVs. Findings from this study indicate that there could also be a transport limit on the validity of defect characterization techniques based on capacitance spectroscopy when studying materials and devices in general beyond OPVs, especially at low temperatures.

ACKNOWLEDGMENT

We thank Prof. William Vandenberghe for his valuable suggestions as well as reading of this manuscript. This work was sponsored by the National Science Foundation (NSF) DMR-1305893. J.W.P.H. acknowledges the support from Texas Instruments Distinguished Chair in Nanoelectronics.

REFERENCE

[1] O. V. Mikhnenko, M. Kuik, J. Lin, N. van der Kaap, T.-Q. Nguyen, and P. W. M. Blom, Trap-Limited Exciton Diffusion in Organic Semiconductors, Adv. Mater. **26**, 1912 (2013).

[2] R. A. Street, J. E. Northrup, and B. S. Krusor, Radiation Induced Recombination Centers in Organic Solar Cells, Phys. Rev. B **85**, 205211 (2012).

[3] R. A. Street, A. Krakaris, and S. R. Cowan, Recombination Through Different Types of Localized States in Organic Solar Cells, Adv. Funct. Mater. **22**, 4608 (2012).

[4] Z. Liang, A. Nardes, D. Wang, J. J. Berry, and B. A. Gregg, Defect Engineering in Π-Conjugated Polymers, Chem. Mater. **21**, 4914 (2009).

[5] P. P. Boix, G. Garcia-Belmonte, U. Muñecas, M. Neophytou, C. Waldauf, and R. Pacios, Determination of Gap Defect States in Organic Bulk Heterojunction Solar Cells From Capacitance Measurements, Appl. Phys. Lett. **95**, 233302 (2009).

[6] S. Neugebauer, J. Rauh, C. Deibel, and V. Dyakonov, Investigation of Electronic

Trap States in Organic Photovoltaic Materials by Current-Based Deep Level Transient Spectroscopy, Appl. Phys. Lett. **100**, 263304 (2012).

[7] J. Schafferhans, A. Baumann, A. Wagenpfahl, C. Deibel, and V. Dyakonov, Oxygen Doping of P3HT: PCBM Blends: Influence on Trap States, Charge Carrier Mobility and Solar Cell Performance, Org. Electron. **11**, 1693 (2010).

[8] C.-Y. Nam, D. Su, and C. T. Black, High-Performance Air-Processed Polymer-Fullerene Bulk Heterojunction Solar Cells Adv. Funct. Mater. **19**, 3552 (2009).

[9] C. T. Sah and V. G. K. Reddi, Frequency Dependence of the Reverse-Biased Capacitance of Gold-Doped Silicon $P^{+}N$ Step Junctions, Electron Devices, IEEE Transactions on **11**, 345 (1964).

[10] E. P. EerNisse, Accurate Capacitance Calculations for Pn Junctions Containing Traps, Appl. Phys. Lett. **18**, 183 (1971).

[11] L. C. Kimerling, Influence of Deep Traps on the Measurement of Free-Carrier Distributions in Semiconductors by Junction Capacitance Techniques, J. Appl. Phys. **45**, 1839 (1974).

[12] T. Walter, R. Herberholz, C. Müller, and H. W. Schock, Determination of Defect Distributions From Admittance Measurements and Application to Cu(in,Ga)Se2 Based Heterojunctions, J. Appl. Phys. **80**, 4411 (1996).

[13] S. S. Hegedus and E. A. Fagen, Midgap States in a-Si:H and a-SiGe:H P-I-N Solar Cells and Schottky Junctions by Capacitance Techniques, J. Appl. Phys. **71**, 5941 (1992).

[14] T. Muntasir and S. Chaudhary, Understanding Defect Distributions in Polythiophenes via Comparison of Regioregular and Regiorandom Species, J. Appl. Phys. **118**, 205504 (2015).

[15] T. Muntasir and S. Chaudhary, Defects in Solution-Processed Dithienylsilole-Based Small-Molecule Photovoltaic Thin-Films, J. Appl. Phys. **119**, 025501 (2016).

[16] S. Khelifi, K. Decock, J. Lauwaert, H. Vrielinck, D. Spoltore, F. Piersimoni, J. Manca, A. Belghachi, and M. Burgelman, Investigation of Defects by Admittance Spectroscopy Measurements in Poly (3-Hexylthiophene):(6,6)-Phenyl C61-Butyric Acid Methyl Ester Organic Solar Cells Degraded Under Air Exposure, J. Appl. Phys. **110**, 094509 (2011).

[17] D. Spoltore, W. D. Oosterbaan, S. Khelifi, J. N. Clifford, A. Viterisi, E. Palomares, M. Burgelman, L. Lutsen, D. Vanderzande, and J. Manca, Effect of Polymer Crystallinity in P3HT:PCBM Solar Cells on Band Gap Trap States and Apparent Recombination Order, Adv. Energy Mater. **3**, 466 (2013).

[18] J. A. Carr, M. Elshobaki, and S. Chaudhary, Deep Defects and the Attempt to Escape Frequency in Organic Photovoltaic Materials, Appl. Phys. Lett. **107**, 203302 (2015).

[19] B. Ecker, J. C. Nolasco, J. Pallarés, L. F. Marsal, J. Posdorfer, J. Parisi, and E. von Hauff, Degradation Effects Related to the Hole Transport Layer in Organic Solar Cells, Adv. Funct. Mater. **21**, 2705 (2011).

[20] M. Samiee, S. Konduri, B. Ganapathy, R. Kottokkaran, H. A. Abbas, A. Kitahara, P. Joshi, L. Zhang, M. Noack, and V. Dalal, Defect Density and Dielectric Constant in Perovskite Solar Cells, Appl. Phys. Lett. **105**, 153502 (2014).

[21] Y. Shao, Z. Xiao, C. Bi, Y. Yuan, and J. Huang, Origin and Elimination of Photocurrent Hysteresis by Fullerene Passivation in CH, Nat. Commun. **5**, 1 (2014).
[22] V. V. Brus, C. M. Proctor, N. A. Ran, and T.-Q. Nguyen, Capacitance Spectroscopy for Quantifying Recombination Losses in Nonfullerene Small‐Molecule Bulk Heterojunction Solar Cells, Adv. Energy Mater. (2016).
[23] E. A. Schiff, R. I. Devlen, H. T. Grahn, J. Tauc, and S. Guha, Picosecond Electron Drift Mobility Measurements in Hydrogenated Amorphous Silicon, Appl. Phys. Lett. **54**, 1911 (1989).
[24] J. Lee, J. D. Cohen, and W. N. Shafarman, The Determination of Carrier Mobilities in CIGS Photovoltaic Devices Using High-Frequency Admittance Measurements, Thin Solid Films **480-481**, 336 (2005).
[25] D. Bartesaghi, I. D. C. Pérez, J. Kniepert, S. Roland, M. Turbiez, D. Neher, and L. J. A. Koster, Competition Between Recombination and Extraction of Free Charges Determines the Fill Factor of Organic Solar Cell, Nat. Commun. **6**, 7083 (2015).
[26] A. Baumann, J. Lorrmann, D. Rauh, C. Deibel, and V. Dyakonov, A New Approach for Probing the Mobility and Lifetime of Photogenerated Charge Carriers in Organic Solar Cells Under Real Operating Conditions, Adv. Mater. **24**, 4381 (2012).
[27] B. Ebenhoch, S. A. J. Thomson, K. Genevicius, G. Juska, and I. D. W. Samuel, Charge carrier mobility of the organic photovoltaic materials PTB7 and PC71BM and its influence on device performance, Org. Electron. **22**, 62 (2015).
[28] L. G. Kaake, P. F. Barbara, and X. Y. Zhu, Intrinsic Charge Trapping in Organic and Polymeric Semiconductors: a Physical Chemistry Perspective, J. Phys. Chem. Lett. **1**, 628 (2010).
[29] T. Kirchartz, W. Gong, S. A. Hawks, T. Agostinelli, R. C. I. MacKenzie, Y. Yang, and J. Nelson, Sensitivity of the Mott–Schottky Analysis in Organic Solar Cells, J. Phys. Chem. C **116**, 7672 (2012).
[30] F. Deledalle, T. Kirchartz, M. S. Vezie, M. Campoy-Quiles, P. Shakya Tuladhar, J. Nelson, and J. R. Durrant, Understanding the Effect of Unintentional Doping on Transport Optimization and Analysis in Efficient Organic Bulk-Heterojunction Solar Cells, Phys. Rev. X **5**, 011032 (2015).
[31] J. Wang, L. Xu, Y.-J. Lee, M. De Anda Villa, A. V. Malko, and J. W. P. Hsu, Effects of Contact-Induced Doping on the Behaviors of Organic Photovoltaic Devices, Nano Lett. **15**, 7627 (2015).
[32] M. Nyman, S. Dahlström, O. J. Sandberg, and R. Österbacka, Unintentional Bulk Doping of Polymer-Fullerene Blends From a Thin Interfacial Layer of MoO3, Adv. Energy Mater. **6**, 1600670 (2016).
[33] G. Dennler, M. C. Scharber, and C. J. Brabec, Polymer-Fullerene Bulk-Heterojunction Solar Cells, Adv. Mater. **21**, 1323 (2009).
[34] Y. Liu, J. Zhao, Z. Li, C. Mu, W. Ma, H. Hu, K. Jiang, H. Lin, H. Ade, and H. Yan, Aggregation and Morphology Control Enables Multiple Cases of High-Efficiency Polymer Solar Cells, Nat. Commun. **5**, 1 (2014).
[35] G. F. A. Dibb, M.-A. Muth, T. Kirchartz, S. Engmann, H. Hoppe, G. Gobsch, M. Thelakkat, N. Blouin, S. Tierney, M. Carrasco-Orozco, J. R. Durrant, and J.

Nelson, Influence of Doping on Charge Carrier Collection in Normal and Inverted Geometry Polymer:Fullerene Solar Cells, Sci. Rep. **3**, (2013).
[36] S. C. Price, A. C. Stuart, L. Yang, H. Zhou, and W. You, Fluorine Substituted Conjugated Polymer of Medium Band Gap Yields 7% Efficiency in Polymer−Fullerene Solar Cells, J. Am. Chem. Soc. **133**, 4625 (2011).
[37] J. Peet, L. Wen, P. Byrne, S. Rodman, K. Forberich, Y. Shao, N. Drolet, R. Gaudiana, G. Dennler, and D. Waller, Bulk Heterojunction Solar Cells with Thick Active Layers and High Fill Factors Enabled by a Bithiophene-Co-Thiazolothiazole Push-Pull Copolymer, Appl. Phys. Lett. **98**, 043301 (2011).
[38] T. Kirchartz, T. Agostinelli, M. Campoy-Quiles, W. Gong, and J. Nelson, Understanding the Thickness-Dependent Performance of Organic Bulk Heterojunction Solar Cells: the Influence of Mobility, Lifetime, and Space Charge, J. Phys. Chem. Lett. **3**, 3470 (2012).
[39] Y.-J. Lee, B. L. Adkison, L. Xu, A. A. Kramer, and J. W. P. Hsu, Comparison of Conventional and Inverted Organic Photovoltaic Devices with Controlled Illumination Area and Extraction Layers, Sol. Energy Mater. Sol. Cells **144**, 592 (2016).
[40] J. G. Tait, U. W. Paetzold, D. Cheyns, M. Turbiez, P. Heremans, and B. P. Rand, Interfacial Depletion Regions: Beyond the Space Charge Limit in Thick Bulk Heterojunctions, ACS Appl. Mater. Interfaces **8**, 2211 (2016).
[41] L. Xu, Y.-J. Lee, and J. W. P. Hsu, Charge Collection in Bulk Heterojunction Organic Photovoltaic Devices: an Impedance Spectroscopy Study, Appl. Phys. Lett. **105**, 123904 (2014).
[42] V. V. Brus, On Impedance Spectroscopy Analysis of Nonideal Heterojunctions, Semicond. Sci. Technol. **27**, 035024 (2012).
[43] J. A. Carr and S. Chaudhary, On Accurate Capacitance Characterization of Organic Photovoltaic Cells, Appl. Phys. Lett. **100**, 213902 (2012).
[44] J. V. Li, A. M. Nardes, Z. Liang, S. E. Shaheen, B. A. Gregg, and D. H. Levi, Simultaneous measurement of carrier density and mobility of organic semiconductors using capacitance techniques, Org. Electron. **12**, 1879 (2011).
[45] J. A. Bartelt, D. Lam, T. M. Burke, S. M. Sweetnam, and M. D. McGehee, Charge-Carrier Mobility Requirements for Bulk Heterojunction Solar Cells with High Fill Factor and External Quantum Efficiency >90%, Adv. Energy Mater. **5**, 1500577 (2015).
[46] A. J. Campbell, D. Bradley, E. Werner, and W. Brütting, Deep Level Transient Spectroscopy (DLTS) of a Poly (P-Phenylene Vinylene) Schottky Diode, Synthetic Metals **111-112,** 273 (2000).
[47] M. Burgelman, P. Nollet, and S. Degrave, Modelling Polycrystalline Semiconductor Solar Cells, Thin Solid Films **361**, 527 (2000).
[48] A. Niemegeers and M. Burgelman, Numerical Modelling of Ac-Characteristics of CdTe and CIS Solar Cells, 25nd IEEE Photovoltaic Specialists Conference, Washington DC, IEEE, New York, 1996 901 (1996).
[49] M. Burgelman, K. Decock, S. Khelifi, and A. Abass, Advanced Electrical Simulation of Thin Film Solar Cells, Thin Solid Films **535**, 296 (2013).
[50] R. A. Street, Electronic Structure and Properties of Organic Bulk‐Heterojunction Interfaces, Adv. Mater. **28**, 3814 (2015).

[51] T. Kirchartz, B. E. Pieters, J. Kirkpatrick, U. Rau, and J. Nelson, Recombination via Tail States in Polythiophene:Fullerene Solar Cells, Phys. Rev. B **83**, 115209 (2011).
[52] Z. He, B. Xiao, F. Liu, H. Wu, Y. Yang, S. Xiao, C. Wang, T. P. Russell, and Y. Cao, Single-Junction Polymer Solar Cells with High Efficiency and Photovoltage, Nat. Photonics **9**, 174 (2015).
[53] T. Ma, K. Jiang, S. Chen, H. Hu, H. Lin, Z. Li, J. Zhao, Y. Liu, Y.-M. Chang, C.-C. Hsiao, and H. Yan, Efficient Low-Bandgap Polymer Solar Cells with High Open-Circuit Voltage and Good Stability, Adv. Energy Mater. **5**, 1501282 (2015).
[54] L. Xu, J. Wang, M. de A. Villa, T. B. Daunis, Y.-J. Lee, A. V. Malko, and J. W. P. Hsu, Quantitative Analyses of Competing Photocurrent Generation Mechanisms in Fullerene-Based Organic Photovoltaics, J. Phys. Chem. C **120**, 16470 (2016).
[55] J. C. Blakesley, F. A. Castro, W. Kylberg, G. F. A. Dibb, C. Arantes, R. Valaski, M. Cremona, J. S. Kim, and J.-S. Kim, Towards reliable charge-mobility benchmark measurements for organic semiconductors Organic Electronics, Org. Electron. **15**, 1263 (2014).
[56] B. Yang, Z. Xiao, and J. Huang, Polymer Aggregation Correlated Transition From Schottky-Junction to Bulk Heterojunction Organic Solar Cells, Appl. Phys. Lett. **104**, 143304 (2014).
[57] M. Zhang, H. Wang, H. Tian, Y. Geng, and C. W. Tang, Bulk Heterojunction Photovoltaic Cells with Low Donor Concentration, Adv. Mater. **23**, 4960 (2011).
[58] C. M. Proctor, A. S. Kher, J. A. Love, Y. Huang, A. Sharenko, G. C. Bazan, and T.-Q. Nguyen, Understanding Charge Transport in Molecular Blend Films in Terms of Structural Order and Connectivity of Conductive Pathways, Adv. Energy Mater. **6**, 1502285 (2016).
[59] B. W. Larson, J. B. Whitaker, X.-B. Wang, A. A. Popov, G. Rumbles, N. Kopidakis, S. H. Strauss, and O. V. Boltalina, Electron Affinity of Phenyl–C 61–Butyric Acid Methyl Ester (PCBM), J. Phys. Chem. C **117**, 14958 (2013).
[60] R. C. I. MacKenzie, C. G. Shuttle, M. L. Chabinyc, and J. Nelson, Extracting Microscopic Device Parameters From Transient Photocurrent Measurements of P3HT:PCBM Solar Cells, Adv. Energy Mater. **2**, 662 (2012).
[61] D. V. Lang, Deep-Level Transient Spectroscopy: a New Method to Characterize Traps in Semiconductors, J. Appl. Phys. **45**, 3023 (1974).
[62] Y. S. Yang, S. H. Kim, J.-I. Lee, H. Y. Chu, L.-M. Do, H. Lee, J. Oh, T. Zyung, M. K. Ryu, and M. S. Jang, Deep-Level Defect Characteristics in Pentacene Organic Thin Films, Appl. Phys. Lett. **80**, 1595 (2002).
[63] J. V. Li, S. W. Johnston, Y. Yan, and D. H. Levi, Measuring Temperature-Dependent Activation Energy in Thermally Activated Processes: a 2D Arrhenius Plot Method, Rev. Sci. Instrum. **81**, 033910 (2010).
[64] See Supplemental Material at [ ] for J-V curves and device parameters of OPV devices with different thicknesses and P3HT concentrations; C-f curve with and without series resistance correction; detailed discussion on C_d to C_g transition; dopant density obtained from C-V curves at different frequencies; drift-diffusion simulations of defect DOS for different mobilities; non-normalized C-f and DOS

data for different P3HT concentration devices; J-V curves of hole-only devices and the fitting parameters; DOS derived from C-f curve for the 20% P3HT OPV and the simulation result.